RESEARCH ARTICLE

ADVANCED FUNCTIONAL MATERIALS
www.afm-journal.de

Bipolarity Induced Gigantic Intrinsic Anomalous Hall Effect in Iterative-Grown Kagome Semimetal $Co_3Sn_2S_2$ Crystals

Senhao Lv, Hui Guo, Wei Jiang, Jiangang Yang, Lin Zhao, Minjun Wang, Hengxin Tan, Roger Guzman, Xianghua Kong, Ke Zhu, Zhen Zhao, Guoyu Xian, Li Huang, Hui Chen, Dongliang Zhao, Xiao Lin, Stephen J. Pennycook, Wu Zhou, Wei Ji, Binghai Yan, Jun He, Xingjiang Zhou,* Haitao Yang,* Feng Liu,* and Hong-Jun Gao**

As a magnetic Weyl semimetal with broken time-reversal symmetry, kagome-lattice $Co_3Sn_2S_2$ hosts a plethora of exotic quantum phenomena due to the interplay between magnetism, electronic correlations, and non-trivial band topology. However, achieving high crystal quality, which is crucial for understanding intrinsic mechanisms and enhancing the physical properties, still remains a significant challenge. Here, the synthesis of ultra-high-quality $Co_3Sn_2S_2$ single crystals is reported via an iterative chemical vapor transport (iterative-CVT) approach, achieving gigantic anomalous Hall conductivity (AHC) of 1600 $\Omega^{-1}cm^{-1}$, anomalous Hall angle (AHA) of 40%, and exceptional carrier mobility and magnetoresistance of 10 490 cm^2 V^{-1} s^{-1} and 2500%. Intriguingly, a striking 65% enhancement of the AHC is observed upon increasing the temperature from 2 to 50 K, attributed to the presence of bipolar carrier contributions from the Weyl bands. Furthermore, an ultra-narrow flat band near the Fermi level is directly visualized by angle-resolved photoemission spectroscopy, suggesting enhanced electron correlations that render the electron concentration and hence AHC highly temperature-dependent. The findings provide a robust material platform to inspire further research into emergent quantum phenomena in magnetic kagome systems.

1. Introduction

Kagome-lattice materials, with their extraordinary electronic structures featuring Dirac points, flat bands, and van Hove singularities, provide versatile platforms for exploring the physics of non-trivial band topology and strong correlations.[1–5] In particular, magnetic kagome materials with the time-reversal symmetry breaking have garnered significant interest due to the interplay between topological electronic states, magnetic orders, and strongly-correlated interactions.[6–9] An outstanding example is the kagome-lattice ferromagnetic Weyl semimetal $Co_3Sn_2S_2$, which exhibits a plethora of exotic phenomena including large anomalous Hall effect (AHE),[10,11] spin-orbit polaron,[12] topological edge/surface state,[13–15] high anomalous Nernst signal,[16] and quantum AHE predicted in the 2D limit,[11,15] to name just a few. So far, great efforts have been devoted to exploring and improving the

---

S. Lv, H. Guo, J. Yang, L. Zhao, R. Guzman, K. Zhu, Z. Zhao, G. Xian, L. Huang, H. Chen, X. Lin, S. J. Pennycook, W. Zhou, X. Zhou, H. Yang, H.-J. Gao
Institute of Physics and University of Chinese Academy of Sciences
Chinese Academy of Sciences
Beijing 100190, P. R. China
E-mail: XJZhou@iphy.ac.cn; htyang@iphy.ac.cn; hjgao@iphy.ac.cn

S. Lv, D. Zhao, J. He
Central Iron & Steel Research Institute
Beijing 100081, P. R. China
E-mail: hejun@cisri.com.cn

W. Jiang, M. Wang
School of Physics
Beijing Institute of Technology
Beijing 100081, P. R. China

H. Tan, B. Yan
Weizmann Institute of Science
Department of Condensed Matter Physics
Rehovot 7610001, Israel

X. Kong
College of Physics and Optoelectronic Engineering
Shenzhen University
Shenzhen 518060, P. R. China

W. Ji
Department of Physics
Renmin University of China
Beijing 100872, P. R. China

F. Liu
Department of Materials Science and Engineering
University of Utah
Salt Lake City, Utah 84112, USA
E-mail: ftiger.liu@utah.edu

The ORCID identification number(s) for the author(s) of this article can be found under https://doi.org/10.1002/adfm.202510587

DOI: 10.1002/adfm.202510587

physical properties of $Co_3Sn_2S_2$, which are crucial for understanding its intrinsic physical mechanisms and for tuning its properties to develop next-generation high-performance electronic and spintronic devices.[17,18] This, however, relies critically on a priori improvement in the quality of $Co_3Sn_2S_2$ crystals.

One of the key electronic transport phenomena is AHE, which arises from two distinct microscopic mechanisms, i.e., an intrinsic one associated with Berry curvature and an extrinsic one driven by scattering processes.[19,20] A known strategy to enhance the AHE in $Co_3Sn_2S_2$ involves chemical doping, which introduces extrinsic contributions from impurity scattering.[21] However, this approach usually suffers from degrading other useful properties such as the mobility and Curie temperature. In addition, the very high mobilities and magnetoresistance typically observed in topological semimetals,[22,23] attributed to the high Fermi velocity of massless Dirac states and uncompensated electron and hole carriers, have yet to be realized in $Co_3Sn_2S_2$ crystals. Moreover, direct visualization of the flat band related to the exotic correlated electron phenomena has not been reported in $Co_3Sn_2S_2$ crystals. Therefore, a significant improvement in crystal quality, thereby a deeper understanding of the magnetic Weyl semimetal, is strongly desired. The synthesis of high-quality kagome-lattice materials remains a major challenge due to issues such as imperfect crystallinity, lattice distortions, vacancies, and impurities.[24,25]

Here, we achieved the growth of large-size, ultra-high-quality $Co_3Sn_2S_2$ single crystals via an iterative chemical vapor transport (denoted as iterative-CVT) approach with crystal granules as the source materials. The ultra-high-quality $Co_3Sn_2S_2$ single crystal, exhibiting an ultra-low impurity density and minimal lattice defects, demonstrates exceptional transport properties, including high carrier mobility, large magnetoresistance (MR), gigantic anomalous Hall conductivity (AHC) and anomalous Hall angle (AHA) of ≈10^4 cm^2 V^{-1} s^{-1}, 2500%, 1600 Ω^{-1} cm^{-1}, and 40%, respectively. These values represent a significant improvement over previously reported highest values for the pristine $Co_3Sn_2S_2$ (2600 cm^2 V^{-1} s^{-1}, 180%, 1130 $\Omega^{-1}cm^{-1}$, and 33%). Notably, the intrinsic AHC is enhanced by nearly 65%, increasing from 980 to 1600 $\Omega^{-1}cm^{-1}$ as the temperature rises from 2 to 50 K. Furthermore, using angle-resolved photoemission spectroscopy (ARPES), we directly visualize an ultra-narrow flat band with a bandwidth of ≈7 meV near the Fermi level. Combining these observations with density functional theory (DFT) calculations, we propose a novel microscopic mechanism, namely an intrinsic bipolar AHE effect arising from the bipolarity of large Berry curvature near the Weyl bands, which underlies the significant enhancement of AHC observed in the ultra-high-quality $Co_3Sn_2S_2$.

2. Iterative-CVT Synthesis Approach

To achieve ultra-high-quality $Co_3Sn_2S_2$ single crystal, we developed an iterative-CVT growth technique (**Figure 1a**). This method enhances crystal quality by using pre-grown crystal granules as source materials instead of raw elements. This iterative growth process enables better stoichiometry control, reduces impurity and defect concentrations, and yields larger, higher-quality single crystals. Initially, irregular-shaped $Co_3Sn_2S_2$ crystals are synthesized via the conventional self-flux method with slow cooling. These single-crystal granules are then used as source materials in an iterative single-crystal-to-single-crystal growth process via CVT, employing NH_4Cl as the transport agent. This refinement cycle further purifies the materials, ultimately producing large-size, regular-shaped, ultra-high-quality $Co_3Sn_2S_2$ single crystals.

The $Co_3Sn_2S_2$ has a rhombohedral structure (space group R-3m, No. 166), wherein Co atoms are arranged into a kagome lattice in the *ab* plane with Sn atoms positioned at the hexagon centers (Figure 1b). A typical $Co_3Sn_2S_2$ single crystal obtained via iterative-CVT exhibits a well-defined hexagonal morphology, with a lateral size of ≈5.5 mm (Figure 1c). Notably, all synthesized $Co_3Sn_2S_2$ crystals display a consistent hexagonal shape, indicating a preferential growth along the *ab* plane, aligned with the Co_3Sn kagome lattice (Figure S1, Supporting Information). In contrast, crystals obtained from the conventional self-flux method are mostly irregular, with lateral sizes ranging from approximately 1 to 3 mm (Figure 1d; Figure S1, Supporting Information).

The use of single-crystal granules as source materials in iterative-CVT process is a crucial aspect of this synthesis approach. We have attempted to synthesize $Co_3Sn_2S_2$ single crystal using elemental Co, Sn, S with NH_4Cl as the transport agent. However, this method failed due to the reaction of Sn halides with the quartz tube (e.g., $2SnX_2 + SiO_2 \rightarrow Si + 2SnOCl_2$, X = F, Cl, Br, I), which prevented the formation of $Co_3Sn_2S_2$. We also tried using $Co_3Sn_2S_2$ crystal powders, obtained by grinding $Co_3Sn_2S_2$ single crystals, as the source materials with NH_4Cl, but this approach only produced small flakes with 0.2–0.8 mm in lateral size (Figure S2a, Supporting Information), maybe due to rapid nucleation. These control experiments highlight that using $Co_3Sn_2S_2$ single-crystal granules as precursors effectively prevents the reaction between $SnCl_2$ and the quartz tube, maintains proper stoichiometry, and ensures optimal growth conditions, which enables the formation of larger, high-crystallinity hexagonal $Co_3Sn_2S_2$ crystals. Furthermore, the choice of NH_4Cl as the transport agent, rather than I_2 commonly used in previous studies, is another key factor in improving the crystal quality. When $Co_3Sn_2S_2$ crystal granules are used with I_2 as the transport agent, the resulting products are small, irregular Co- and S-deficient granules with normalized atomic ratio Co:Sn:S = 1.23:2.00:1.49 (Figure S2b,c, Supporting Information).

3. Structural Characterizations

We then performed detailed structural characterizations on the $Co_3Sn_2S_2$ single crystals synthesized via the iterative-CVT approach. Elemental analysis of multiple samples confirms an atomic ratio of Co:Sn:S very close to 3:2:2 (Figure S3, Supporting Information). The x-ray diffraction (XRD) pattern exclusively shows the (*00l*) diffraction peaks, verifying the phase purity of the synthesized crystals (Figure S4, Supporting Information). The x-ray rocking curve of the (003) Bragg reflection reveals a significantly smaller full width at half maximum (FWHM) of 0.058° for the iterative-grown $Co_3Sn_2S_2$ compared to 0.105° for crystals fabricated via the self-flux method (**Figure 2a**). Furthermore, the *h0l* plane diffraction pattern displays sharp, unsplit diffraction spots (Figure 2b; Figure S5, Supporting Information), demonstrating high crystallinity and a low density of lattice defects.

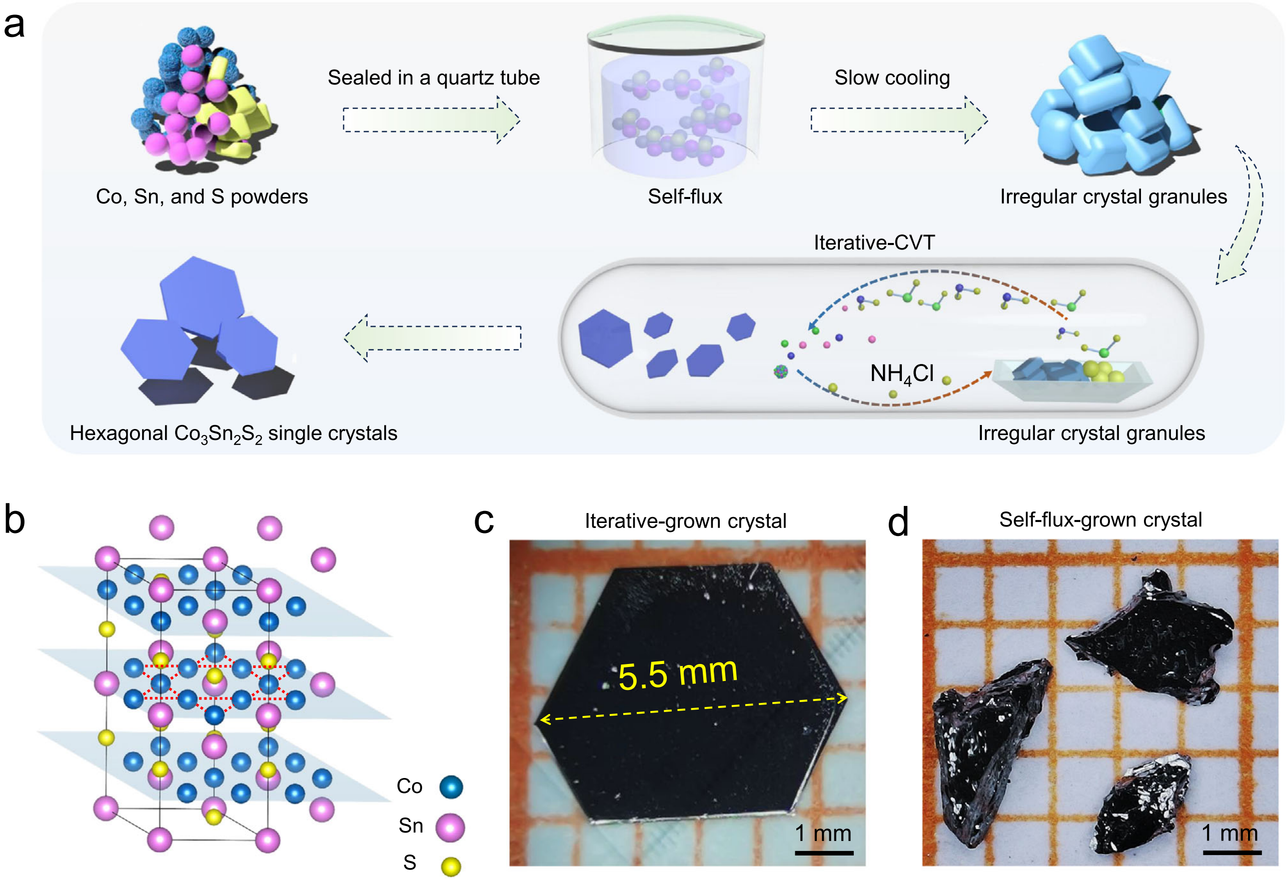

Figure 1. Synthesis of $Co_3Sn_2S_2$ crystals by iterative-CVT approach. a) Schematic illustration of the iterative-CVT growth procedure. The $Co_3Sn_2S_2$ crystal granules, synthesized by the self-flux method, are placed in the high-temperature zone with NH_4Cl as the transport agent. Large-size, hexagonal-shaped $Co_3Sn_2S_2$ single crystals are collected in the low-temperature zone. b) Crystal structure of $Co_3Sn_2S_2$ in a hexagonal setting, consisting of two hexagonal layers of S and Sn as well as a Co_3Sn kagome layer sandwiched between the S planes. Blue, pink, and yellow balls represent Co, Sn, and S atoms, respectively. c) An optical photograph of a synthesized hexagonal-shaped $Co_3Sn_2S_2$ single crystal via the iterative-CVT approach, showing the lateral size of ≈5.5 mm. d) An optical photograph of the irregular-shaped $Co_3Sn_2S_2$ single crystal synthesized by the self-flux method.

To further assess the crystal quality, we carried out the atomic-scale structural analysis using aberration-corrected scanning transmission electron microscopy (STEM) on cross-sectional samples. Figure 2c,d shows simultaneously collected high-angle annular dark-field (HAADF) image and annular bright-field (ABF) STEM images along the [001] zone axis, overlaid with the structural model and indexed Co_3Sn kagome plane, revealing a well-ordered *ab*-plane with a hexagonal lattice. Similarly, Figure 2e,f shows HAADF and ABF images along the [100] zone axis, with the corresponding structural model and indexed main crystallographic planes. Atomic-resolution chemical mapping (Figure 2g) further confirms the distinct spatial distributions of Co, Sn, and S atoms. While aberration-corrected STEM imaging can achieve high spatial resolution (0.5 Å at 300 kV), it generally suffers from limited sampling, which, however, could be partially overcome by combining macroscopic techniques such as XRD for a more comprehensive structural assessment. Thus, these results consistently demonstrate the defect-free, high-crystallinity structure of the $Co_3Sn_2S_2$ crystal. Additionally, scanning tunneling microscopy (STM) is used to quantify the impurities and defects, showing that the impurity density in iterative-grown $Co_3Sn_2S_2$ single crystals is significantly lower than that in self-flux-grown samples (Figure S6, Supporting Information). These structural characterizations collectively confirm the superior quality of the iterative-grown $Co_3Sn_2S_2$ single crystals.

The iterative-CVT method yields significantly higher-quality $Co_3Sn_2S_2$ single crystals compared to the conventional self-flux method, mainly attributed to three key advantages. First, the use of non-volatile NH_4Cl ensures a high vacuum level (4×10^{-5} Pa) and a stable growth temperature, providing a clean and controlled environment that promotes the preferential (00*l*) plane growth while preventing contamination from flux residues and trapped air. Second, employing $Co_3Sn_2S_2$ crystal granules as precursors avoids unwanted reactions between Sn halide and the quartz tube, while also maintaining an optimal precursor concentration and growth rate, thereby ensuring the precise stoichiometry of Co, Sn, and S. Third, the transport agent NH_4Cl, with its higher electronegativity, enhances the transport rate compared to I_2, leading to a greater precursor feedstock concentration in the growth zone and ultimately enabling the synthesis of larger-sized, higher-quality $Co_3Sn_2S_2$ single crystals.[26]

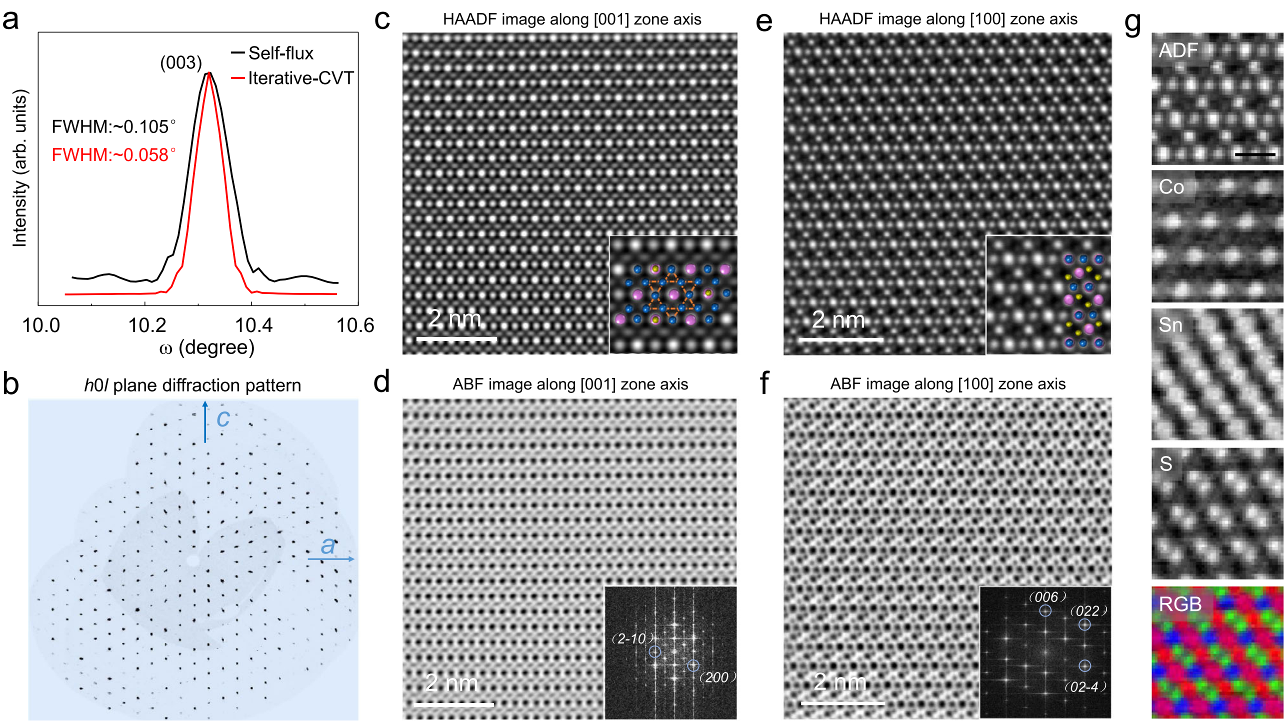

Figure 2. Structural characterizations of iterative-grown $Co_3Sn_2S_2$ crystals. a) X-ray rocking curves of the (003) reflection for $Co_3Sn_2S_2$ single crystals prepared by self-flux (black) and iterative-CVT (red) methods, showing a significantly smaller FWHM of 0.058° for the $Co_3Sn_2S_2$ prepared by the iterative-CVT approach. b) *h0l* plane diffraction pattern of the iterative-grown $Co_3Sn_2S_2$ single crystals, showing sharp diffraction spots without splitting. c,d) Simultaneously acquired high-resolution HAADF (c) and ABF (d) STEM images along the [001] zone axis of the iterative-grown $Co_3Sn_2S_2$ single crystal, respectively. The inset in (c) is a close-up image with overlayed atomic model, where blue, pink, and yellow balls represent the Co, Sn, and S atoms, respectively. The inset in (d) is the FFT pattern with indexed crystallographic planes. e,f) Simultaneously acquired high-resolution HAADF (e) and ABF (f) STEM images along the [100] axis of the iterative-grown $Co_3Sn_2S_2$ single crystal, respectively. g) EELS elemental mapping of the Co-L, Sn-M, and S-L edges, acquired simultaneously with the ADF image, showing the elemental distributions. The RGB false-color map highlights the spatial distribution of Co (blue), Sn (red), S (green) elements.

4. Ultra-Narrow Flat Band

To study the electronic structure of the ultra-high-quality $Co_3Sn_2S_2$ single crystal, we perform high-resolution vacuum ultraviolet (VUV) laser ARPES measurements.[27] The Fermi surface mapping shows six small pockets surrounding the Brillouin zone center Γ (**Figure 3a**), which is in excellent agreement with the DFT calculated projections (Figure 3b). To elucidate the origin of the strong spectral weight near the Brillouin zone corner K(K′), we analyze the electronic dispersion along two momentum cuts (Cut1 and Cut2, Figure 3a). Along the Γ-K direction (Cut1), the band structure near the E_F exhibits topological surface state (TSS, Figure 3c), which is more clearly discernible in the second derivative spectrum. The TSS, located ≈0.4 Å^{-1} from the K point, is consistent with the previous report.[28]

Remarkably, along the momentum Cut2, we observe a nearly dispersionless flat band spreading over a broad momentum range around the K point, as clearly visualized in the second derivative spectra (Figure 3d). The corresponding energy distribution curves (EDCs) exhibit sharp peaks with linewidths below 10 meV near the Fermi level (Figure 3e). Considering the thermal broadening (≈7 meV at 20 K), the intrinsic linewidth is estimated to be 6–7 meV. The experimental results show good consistency with the DFT calculated electronic structure (Figure 3f), further indicating the existence of the flat band. Such an isolated ultra-narrow flat band directly visualized by ARPES in a ferromagnetic kagome semimetals[29] is somewhat surprising, because *d*-orbital flat bands in kagome metals are generally expected to be weak localized or hybridized due to improper orbital symmetry and weak crystal field effects.[30] The emergence of this ultra-narrow flat band could be facilitated by the exceptionally high quality of the iterative-grown $Co_3Sn_2S_2$ single crystals, providing a promising platform for further exploring strongly-correlated phenomena such as orbital diamagnetism.[31]

5. Gigantic Anomalous Hall Effect

We next study the transport properties of the ultra-high-quality $Co_3Sn_2S_2$ single crystals. Magnetization measurements reveal a ferromagnetic transition at a Curie Temperature (T_c) of 177 K (Figure S7, Supporting Information), in agreement with the heat capacity results (Figure S8, Supporting Information). The temperature-dependent resistivity exhibits a distinct kink at T_c = 181 K (**Figure 4a**), indicative of the ferromagnetic transition. The residual resistivity ratio (RRR, ρ_{300K}/ρ_{2K}) exceeds 128, and the conductivity reaches 2.3×10^5 $\Omega^{-1}cm^{-1}$ at 2 K (Figure S9a, Supporting Information), both approximately an order of magnitude higher than previously reported values,[10,11,32]

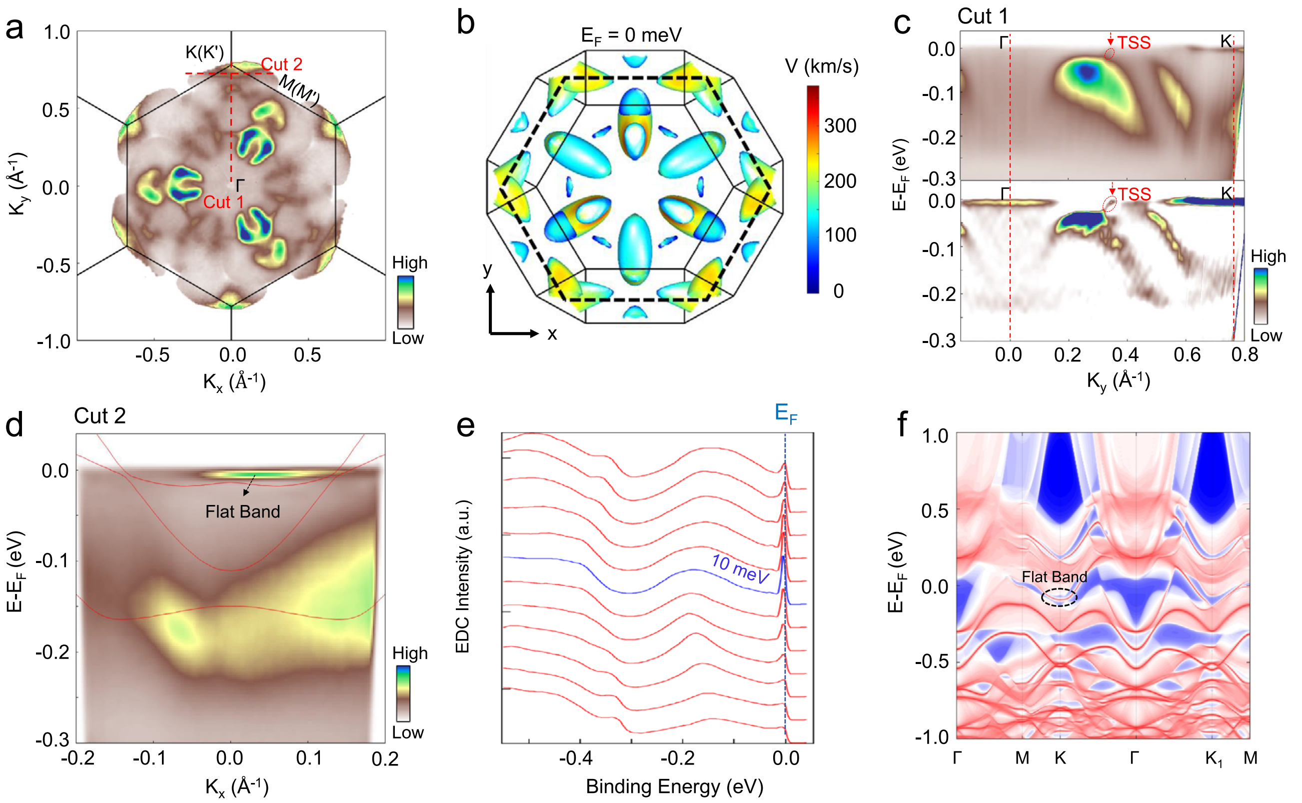

Figure 3. Ultra-narrow flat band and topological surface state near the Fermi level. a) Fermi surface mapping acquired by integrating the spectra weight within a ±10 meV energy window relative to the Fermi level. The red dash lines along K_y and K_x denote momentum cuts, Cut 1 and Cut 2, respectively. b) DFT calculated Fermi surface projections, showing good agreement with the experimental data in (a). The black lines outline the Brillouin zone. c) Band structure along Cut 1 in (a), with the corresponding second derivative spectrum, showing the existence of TSS marked by the red arrow. d) Band structure along Cut 2 in (a), showing a nearly dispersionless flat band near the Fermi level around the K point. e) EDCs along Cut 2 at different K_x positions, showing an ultra-narrow coherent peak corresponding to the flat band, indicating a large DOS near the Fermi level. f) Calculated band dispersions along different high-symmetry directions on the Sn-terminated surface of $Co_3Sn_2S_2$, showing a nearly flat band (circled) near the Fermi level around the K point, in good agreement with the experimental observations in (d).

indicating the exceptional sample quality. Remarkably, a magnetic-field-induced resistivity upturn at low temperatures suggests a pronounced magnetoresistance effect and high carrier mobility.[33,34]

The magneto-transport measurements under out-of-plane magnetic fields reveal a non-saturating positive *MR* of up to 2500% at 2 K (Figure 4b), significantly surpassing previously reported values of 55–250%.[11,35,36] This substantially non-saturating *MR* is attributed to high carrier mobility and electron-hole compensation in $Co_3Sn_2S_2$ single crystals. As the temperature increases to ≈100 K, the magnetoresistance gradually becomes negative due to the magnetic-field induced suppression of thermal spin fluctuations.[11,32] Furthermore, an in-plane negative *MR* (Figure S9d, Supporting Information) and a planar Hall effect (Figure S10, Supporting Information) are observed, consistent with the chiral anomaly associated with Weyl fermions.[32,37] By fitting the transverse and longitudinal conductivity using the semiclassical Drude model (Figure S11, Supporting Information), we extract the carrier densities of electrons and holes at 2 K are $\approx 7.9 \times 10^{19}$ cm^{-3} and 2.2×10^{20} cm^{-3}, respectively, demonstrating a bipolar transport characteristic. The corresponding carrier mobilities for electrons and holes are 10 490 ± 45 cm^2 V^{-1} s^{-1} and 2504 ± 8 cm^2 V^{-1} s^{-1} (Figure 4c), exceeding those of most reported magnetic topological semimetals (e.g., $Co_3Sn_2S_2$ ≈2600 cm^2 V^{-1} s^{-1}, $MnBi_2Te_4$ ≈3110 cm^2 V^{-1} s^{-1}, GaPtBi ≈1500 cm^2 V^{-1} s^{-1}, and Co_2MnGa ≈35 cm^2 V^{-1} s^{-1}).[35,38–40] The ultra-high carrier mobility and large, non-saturating *MR* further corroborate the superior quality of the iterative-grown $Co_3Sn_2S_2$ single crystals.

We further study the AHE. The magnetic-field-dependent Hall resistivity (ρ_{yx}) at different temperatures indicates the coexistence of the AHE and a normal Hall effect with a nonlinear profile (Figure S12, Supporting Information), indicative of a two-carrier conduction mechanism. The total Hall conductivity (σ_{yx}) at 2 and 50 K (Figure 4d) reveals a pronounced AHC σ_{yx}^A, which shows a strong temperature dependence (Figure 4e; Figures S13–S15, Supporting Information). Notably, the σ_{yx}^A reaches 980 Ω^{-1} cm^{-1} at 2 K and increases to a maximum of ≈1600 Ω^{-1} cm^{-1} at 50 K, a nearly 65% enhancement that deviates from previous reports.[11] This increase in AHC at low temperatures is attributed to the electron-hole compensation, as discussed in the theoretical analysis below. Furthermore, the AHA ($\sigma_{yx}^A/\sigma_{xx}$) exceeds 30% across a wide temperature range from 100 to 160 K and reaches a maximum of ≈40% at 140 K (Figure 4f), indicating a gigantic AHE in the ultra-high-quality $Co_3Sn_2S_2$ single crystals. Compared to

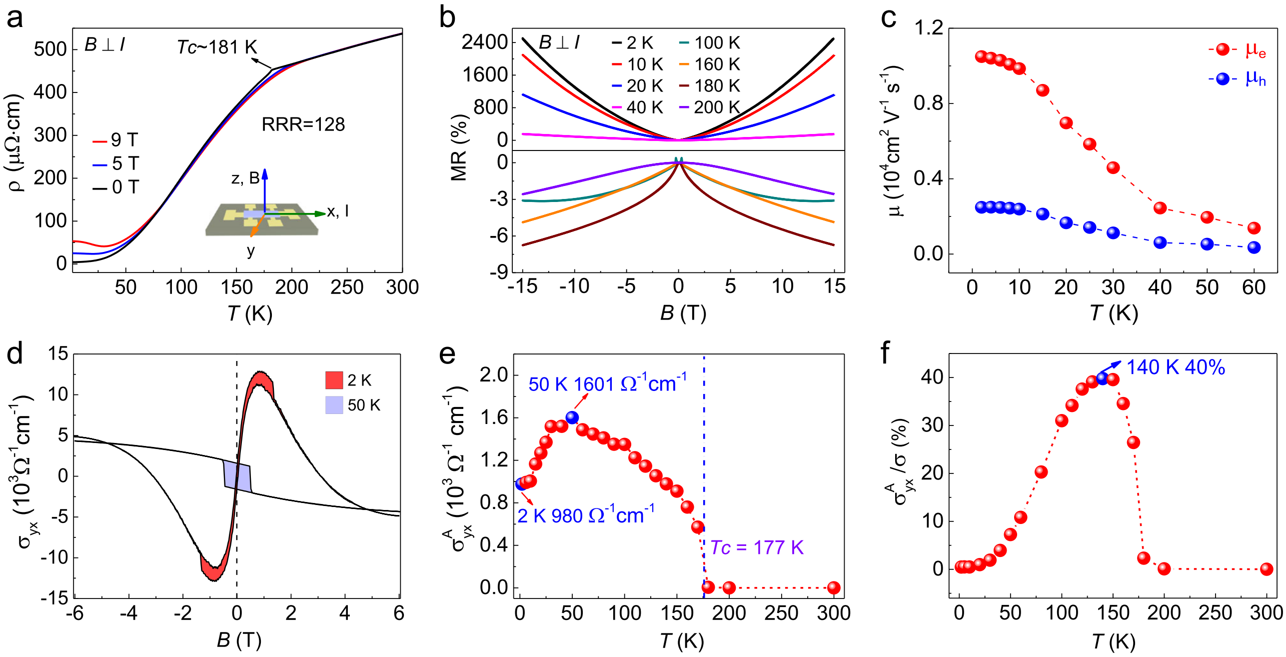

Figure 4. High carrier mobility and gigantic AHE. a) Temperature-dependent resistivity under various magnetic fields along *c* axis, showing a ferromagnetic transition at 181 K and a magnetic-field-induced upturn at low temperatures. b) Magnetoresistance under out-of-plane magnetic fields from −15 T to 15 T at different temperatures, showing a non-saturating positive MR below 100 K and a non-saturating negative MR above 100 K. c) Temperature dependence of carrier mobilities (μ_e and μ_h), showing the maximum mobility of 10 490 ± 45 and 2504 ± 8 cm^2 V^{-1} s^{-1} for electron and hole at 2 K, respectively. d) Magnetic-field-dependent Hall conductivity (σ_{yx}) at 2 and 50 K under out-of-plane magnetic fields, showing hysteresis behaviors associated to AHE. The contribution of AHE is highlighted by shaded areas. e) Temperature dependences of the AHC (σ_{yx}^A), showing a maximum of 1600 Ω^{-1}cm^{-1} at 50 K. f) Temperature dependence of the AHA (σ_{yx}^A/σ) at zero magnetic field, showing a maximum of 40% at 140 K.

the previously reported $Co_3Sn_2S_2$ and other magnetic topological materials,[41–48] the carrier mobility, *MR*, AHC, and AHA of the present $Co_3Sn_2S_2$ single crystals are among the highest (Figures S16 and S17, Supporting Information).

6. Bipolarity Induced Gigantic Intrinsic AHE

One of the most striking properties of our high-quality $Co_3Sn_2S_2$ single crystal is its gigantic AHE, where the AHC exhibits a remarkable 65% increase from 980 to 1600 Ω^{-1} cm^{-1} as the temperature rises from 2 to 50 K. Typically, AHE originates from two distinct microscopic mechanisms, i.e., intrinsic contribution driven by Berry curvature and extrinsic component arising from scattering effects.[19,20] The extrinsic AHE in $Co_3Sn_2S_2$ is generally induced by chemical doping, which introduces considerable impurity scattering.[21] However, given the exceptionally high purity of the iterative-gown $Co_3Sn_2S_2$, the extrinsic contribution is negligible. Moreover, the negative scaling exponent (significantly <1) between σ_H^A and σ_{xx}, together with the large σ_{xx} values that firmly situate the system within the intrinsic regime (Figure S15d, Supporting Information), suggests that the anomalous Hall effect in $Co_3Sn_2S_2$ is dominated by the intrinsic Berry curvature, rather than the extrinsic skew scattering. For magnetic Weyl semimetal like this one, the intrinsic AHE is governed by the Berry curvature of occupied bands near the Weyl nodes.[49,50] Interestingly, the conduction and valence bands around the nodal ring exhibit opposite Berry curvature values,[19,20] implying that carries of opposite polarity (electrons versus holes) can contribute compensating effects to the intrinsic AHE. Consequently, the overall Berry curvature can be tuned in the presence of bipolar transport when the relative carrier concentration changes.

To verify this hypothesis, we analyze the temperature dependence of the carrier concentration. Remarkably, the hole concentration remains nearly constant, whereas the electron concentration gradually decreases as the temperature increases from 2 to 50 K (**Figure** 5a). We attribute this reduction in electron concentration to the presence of the ultra-narrow flat band near the Fermi level in the high-quality $Co_3Sn_2S_2$ single crystal. The nearly dispersionless nature of this flat band implies a strong suppression of electron kinetic energy due to destructive the quantum interference within the kagome lattice,[51] which would significantly enhance electron correlations and modulating the electron density through the electron-electron separation.[52,53] This, in turn, may underlie the observed temperature-dependent electron depletion.

To gain deeper insight, we perform first-principles calculations of the electronic structures of $Co_3Sn_2S_2$ along high-symmetry *k*-paths (Figure 5b). Without SOC, two linear band crossings appear along the U-L and L-Γ paths, situated above and below the Fermi level, respectively, highlighting the coexistence of electron and hole carriers. Due to mirror symmetry, these band crossings form a nodal ring within the mirror plane, while the C_3 symmetry results in six nodal rings within the Brillouin zone (Figure 5c,d). Upon introducing SOC, the nodal rings are gapped, except

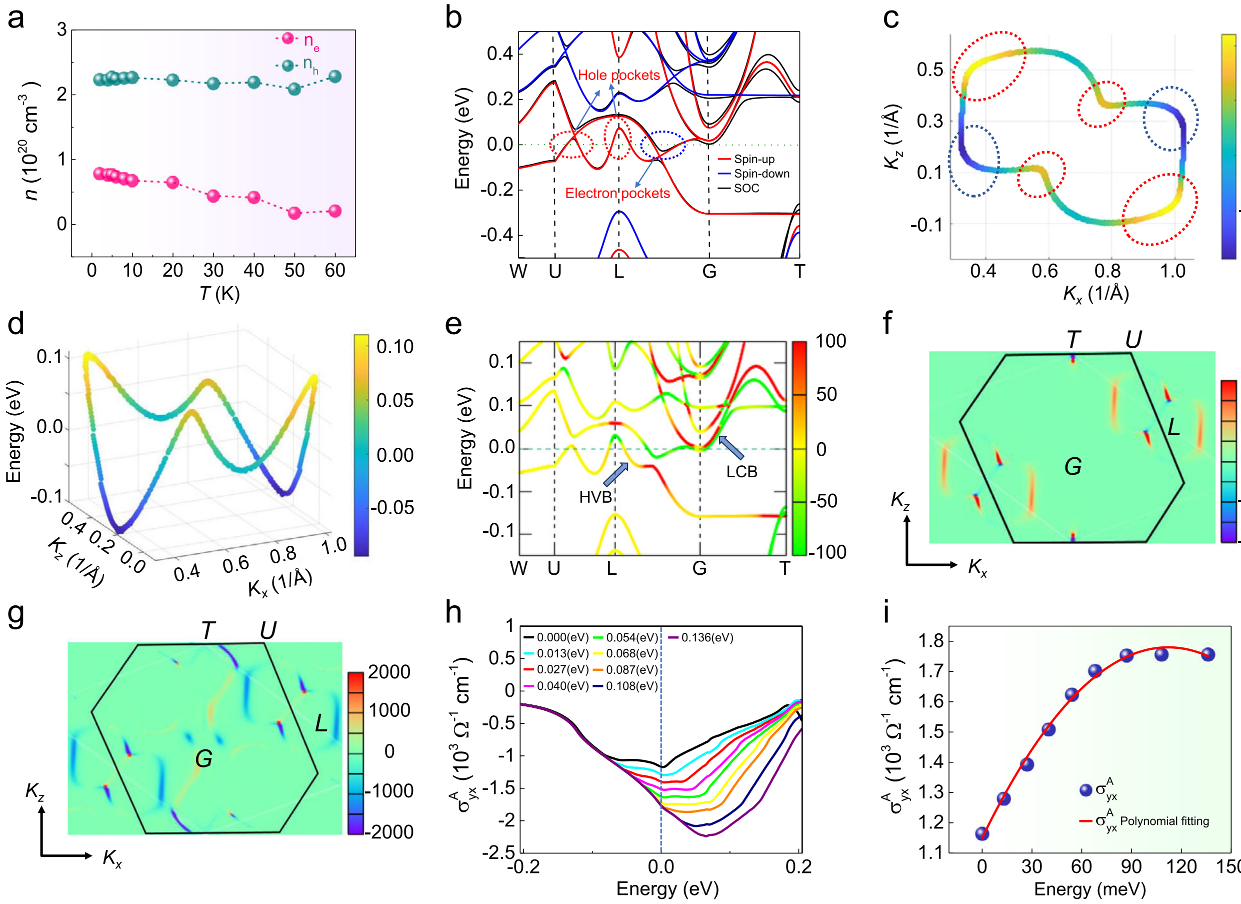

Figure 5. Bipolarity of AHE in the ultra-high-quality $Co_3Sn_2S_2$ crystals. a) Temperature dependence of the electron and hole concentrations, showing that the hole concentration remains nearly constant, while the electron concentration gradually decreases as the temperature increases from 2 to 50 K. b) Electronic band structures of $Co_3Sn_2S_2$ with and without SOC, showing that the Fermi level intersects the spin-up electron energy bands, while the spin-down states exhibit an insulating gap, indicating a half-metallic nature. c) Distribution of the nodal ring in the $k_y = 0$ plane of the reciprocal space. The red and blue dashed circles denote the regions with energies above and below the Fermi level, respectively. d) Energy distribution associated with the nodal ring. e) Berry curvature distribution along the high-symmetry momentum paths. f,g) Berry curvature distribution in the $k_y = 0$ plane corresponding to the LCB and the HVB, respectively. h) AHC as a function of chemical potential under different electron concentrations, modeled by shifting the energy of LCB. i) AHC at the Fermi level as a function of energy shift, as extracted from (h).

for two remaining gapless crossings, which evolve into Weyl points of opposite chirality located ≈60 meV above the Fermi level.

We further calculate the band-resolved Berry curvature along high-symmetry *k*-paths (Figure 5e). Berry curvature originates from SOC-induced band entanglement upon breaking spatial-inversion or time-reversal symmetry. The SOC-induced gap opening at the nodal ring sites generate significant Berry curvature near the Fermi level. To illustrate this effect, we focus on a representative nodal ring in the $k_y = 0$ plane. The Berry curvature distributions for the highest valence band (HVB) and lowest conduction band (LCB) (Figure 5f,g) reveal strong Berry curvature accumulation around the original nodal ring. This results in a peak in AHC near the Fermi energy (Figure 5h), consistent with previous calculations.[54] More importantly, the HVB and LCB exhibit opposite Berry curvature contributions near the nodal ring, reinforcing their bipolar influence on the AHE, since both bands cross the Fermi level. This is further corroborated by our band-resolved AHC calculations, which show opposite contributions for all occupied states below the LCB versus the LCB itself (Figure S18, Supporting Information).

Given the bipolar nature of the AHC from the LCB and HVB, we thus attribute the observed AHC enhancement to the depletion of electron carriers within the LCB-derived electron pocket near the Fermi surface. As the Berry curvature contribution from the LCB diminishes, while the opposite contribution from the HVB remains unchanged, the net AHC increases with increasing temperature, in good agreement with our experimental findings. This is further supported by the theoretical modeling, where we simulate a decrease in electron occupation within the LCB while keeping all other bands constant (Figure 5h,i; Figures S18 and S19, Supporting Information). The absolute AHC value increases and eventually saturates as electron depletion. Notably, the theoretical calculations predict a nearly 50% enhancement in AHC at the Fermi level, from −1165 to −1757 S cm^{-1}, closely matching the experimental observations. Interestingly, an even larger AHC enhancement, approaching 2500 S cm^{-1}, is predicted ≈0.1 eV above the Fermi level.

7. Conclusion

We have successfully synthesized large-size, ultra-high-quality $Co_3Sn_2S_2$ single crystals with an ultra-low impurity density by using an iterative-CVT approach. The enhanced crystal quality leads to a significant improvement in key electrical transport properties, including carrier mobility, *MR*, and AHE. Notably, we observe an unusual ≈65% enhancement of the AHC with increasing temperature in the low-temperature regime, which stems from the bipolar nature of Berry curvature near the Weyl nodes, strongly associated with the relative carrier densities of electrons versus holes. Furthermore, we directly visualize an ultra-narrow flat band near the Fermi level, which enhances the Berry curvature at the Weyl nodes and renders the electron concentration highly temperature-dependent. This discovery suggests the potential for tuning the AHE, possibly even achieving the quantum AHE, by electrical gating in low-dimensional $Co_3Sn_2S_2$. Our work not only establishes an effective route for synthesizing high-quality magnetic topological materials but also opens new avenues for exploring exotic quantum phenomena in topological and kagome-lattice systems.

8. Experimental Section

Synthesis of the $Co_3Sn_2S_2$ Single Crystals: Ultra-high-quality $Co_3Sn_2S_2$ single crystals were successfully synthesized via an iterative chemical vapor transport approach using single-crystal granules as source materials. Initially, irregularly-shaped $Co_3Sn_2S_2$ single crystals were prepared using the conventional self-flux method. Stoichiometric amounts of Co, Sn, and S, in a molar ratio of Co:Sn:S = 3:2:2, were mixed and placed in a crucible, then sealed in a quartz tube under high vacuum using a high temperature flame gun. The sealed tube was slowly heated to 1000 °C over 55 h, after which the temperature was stabilized for 72 h before a slow cooling to 600 °C at 2 °C/h. Subsequently, the as-grown single-crystal granules were enclosed in a quartz tube with NH_4Cl as the transport agent and subjected to an iterative-CVT process. Large-size, high-quality hexagonal $Co_3Sn_2S_2$ single crystals were obtained under a temperature gradient of 1000 °C to 900 °C over one week. This iterative-CVT approach offers a universal strategy for synthesizing other kagome materials with improved crystal quality and superior physical properties. Notably, this technique was successfully extended to synthesize high-quality $Co_3In_2S_2$ and $Ni_3In_2S_2$ single crystals, which exhibit excellent transport performance (Figures S20 and S21, Supporting Information).

Sample Characterizations: XRD measurements were carried out at room temperature on a Rigaku SmartLab SE diffractometer using Cu Kα radiation ($\lambda = 0.15\,418$ nm). Single-crystal X-ray diffraction data and rocking curves were recorded with a Bruker D8 Venture system. Morphological analysis and elemental composition were examined by scanning electron microscopy (SEM) and energy-dispersive X-ray spectroscopy (EDS) on a HITACHI S5000 microscope equipped with a Bruker XFlash 6|60 detector. STEM and EELS measurements were carried out using a Nion HERMES-100, operated at 100 kV and a probe forming semi-angle of 30 mrad. STM measurements were carried out in a Createc low-temperature system at 4.2 K with a base pressure below 3.0×10^{-10} mbar.[12] Magnetization measurements were performed on well-oriented single crystals with magnetic fields applied along the *a* and *c* axes, using a Magnetic Property Measurement System (MPMS 3, Quantum Design). Electrical transport properties were measured using a Physical Property Measurement System (PPMS, Quantum Design, 15 T). ARPES measurements were conducted at 20 K using an ultraviolet laser as the excitation source, equipped with a photon energy of $h\nu = 6.994$ eV with a bandwidth of 0.26 meV.[27]

DFT Calculations: Density functional theory (DFT) calculations were conducted employing the Vienna ab-initio Simulation Package (VASP).[55] The exchange and correlation energies were treated under the generalized gradient approximation, following the Perdew–Burke–Ernzerhof (PBE) scheme.[56] The electronic relaxation process employed a Gamma-centered Monkhorst-Pack k-point grid of 11×11×11,[57] an energy cutoff of 500 eV, and a total energy convergence tolerance set to 10^{-5} eV. PBE pseudopotentials were adopted in all calculations, treating nine valence electrons for Co(d^8s^1), fourteen valence electrons for Sn($d^{10}s^2p^2$), and six valence electrons for S(s^2p^4).

To investigate the topological properties of $Co_3Sn_2S_2$, we employed the wannier90 package[58] to fit the DFT calculated electronic band structure. Based on the projected density of states analysis, the dominant contributions around the Fermi level are attributed to the *d* orbitals of Cobalt and the *p* orbitals of Tin and Sulfur. Consequently, these orbitals were selected as the Wannier functions for the energy band fitting. The Wanniertools package[59] was used to compute the Berry curvature distribution and the AHC using the Kubo formula[60] shown below

$$\sigma_{xy} = -\frac{e^2}{\hbar} \int \frac{dk}{(2\pi)^3} \sum_n f_{nk} \Omega_n^z (k) \tag{1}$$

$$\Omega_n^z \ (\mathrm{k}) = -\sum_{\mathrm{n}' \neq \mathrm{n}} \frac{2\mathrm{Im}\left[\left\langle \mathrm{u_{nk}} \left| \mathrm{v_{xk}} \right| \mathrm{u_{n'k}} \right\rangle \left\langle \mathrm{u_{n'k}} \left| \mathrm{v_{yk}} \right| \mathrm{u_{nk}} \right\rangle\right]}{\left(\varepsilon_{\mathrm{n'k}} - \varepsilon_{\mathrm{nk}}\right)^2} \tag{2}$$

where f_{nk} denotes the Fermi-Dirac occupation function and $\Omega_n^z(\mathrm{k})$ is the *z* component Berry curvature. To simulate the influence of the decreased electron carrier concentration, we assume a small energy shift of the lowest conduction band to change the electron occupation while maintaining the Fermi level and all the other bands unchanged.

We calculated the density of states N(E) corresponding to LCB as well as HVB and used following equation to calculate the hole and electron concentration corresponding to HVB and LCB, respectively, as a function of Fermi energy,

$$\mathrm{n} = \frac{1}{\mathrm{V_{cell}}} \int \mathrm{N(E)\, f(E)\, dE} \tag{3}$$

Supporting Information

Supporting Information is available from the Wiley Online Library or from the author.

Acknowledgements

The authors would like to thank Prof. Enke Liu and Prof. Gang Su for valuable discussions. The work was supported by grants from the National Key Research and Development Projects of China (2022YFA1204100, 2022YFA1403900), the National Natural Science Foundation of China (62488201, 12204037, 11974422, 12104313), the Chinese Academy of Sciences (XDB33030100), the Innovation Program of Quantum Science and Technology (2021ZD0302700), F.L. acknowledges National Science Foundation of U.S.A. (#2326228).

Conflict of Interest

The authors declare no conflict of interest.

Author Contributions

S.L., H.G., W.J., and J.Y. contributed equally to this work. H.-J.G. designed the project. H.T.Y., S.H.L., and K.Z. prepared the samples. S.H.L., J.H., and H.T.Y. performed the magnetization measurements. S.H.L., H.G., G.Y.X.,

Z.Z., and H.T.Y. performed the transport experiments. H.C., and L.H. performed the STM experiments with the guidance of H.-J.G. R.G. and W.Z. performed the STEM experiments. F.L. participated in the analysis of experimental and computational results, and in writing the paper. W.J, M.J.W., H.X.T, X.H.K., W.Ji, and B.H.Y. performed the DFT calculations. J.G.Y, L.Z., and X.J.Z. perform the ARPES experiments. All authors participated in the data analysis and manuscript writing.

Data Availability Statement

The data that support the findings of this study are available from the corresponding author upon reasonable request.

Keywords

anomalous hall conductivity, bipolarity, $Co_3Sn_2S_2$ single crystals, iterative-CVT, ultra-narrow flat band

Received: April 27, 2025
Revised: June 18, 2025
Published online:

---

[1] Z. F. Wang, N. H. Su, F. Liu, *Nano Lett.* **2013**, *13*, 2842.
[2] T. Kambe, R. Sakamoto, K. Hoshiko, K. Takada, M. Miyachi, J. H. Ryu, S. Sasaki, J. Kim, K. Nakazato, M. Takata, H. Nishihara, *J. Am. Chem. Soc.* **2013**, *135*, 2462.
[3] A. Y. Gao, Y. F. Liu, C. W. Hu, J. X. Qiu, C. Tzschaschel, B. Ghosh, S. C. Ho, D. Bérubé, R. Chen, H. P. Sun, Z. W. Zhang, X. Y. Zhang, Y. X. Wang, N. Z. Wang, Z. M. Huang, C. Felser, A. Agarwal, T. Ding, H. J. Tien, A. Akey, J. Gardener, B. Singh, K. Watanabe, T. Taniguchi, K. S. Burch, D. C. Bell, B. B. Zhou, W. B. Gao, H. Z. Lu, A. Bansil, et al., *Nature* **2021**, *595*, 521.
[4] O. Breunig, Y. Ando, *Nat. Rev. Phys.* **2021**, *4*, 184.
[5] Y. J. Wang, H. Wu, G. T. McCandless, J. Y. Chan, M. N. Ali, *Nat. Rev. Phys.* **2023**, *5*, 635.
[6] C.-Z. Chang, C. X. Liu, A. H. MacDonald, *Rev. Mod. Phys.* **2023**, *95*, 011002.
[7] J. X. Yin, B. Lian, M. Z. Hasan, *Nature* **2022**, *612*, 647.
[8] X. K. Li, J. Koo, Z. W. Zhu, K. Behnia, B. H. Yan, *Nat. Commun.* **2023**, *14*, 1642.
[9] J.-X. Yin, W. L. Ma, T. A. Cochran, X. T. Xu, S. S. Zhang, H.-J. Tien, N. Shumiya, G. M. Cheng, K. Jiang, B. Lian, Z. D. Song, G. Q. Chang, I. Belopolski, D. Multer, M. Litskevich, Z.-J. Cheng, X. P. Yang, B. Swidler, H. B. Zhou, H. Lin, T. Neupert, Z. Q. Wang, N. Yao, T.-R. Chang, S. Jia, M. Z. Hasan, *Nature* **2020**, *583*, 533.
[10] Q. Wang, Y. F. Xu, R. Lou, Z. H. Liu, M. Li, Y. B. Huang, D. W. Shen, H. M. Weng, S. C. Wang, H. C. Lei, *Nat. Commun.* **2018**, *9*, 4212.
[11] E. K. Liu, Y. Sun, N. Kumar, L. Muechler, A. Sun, L. Jiao, S.-Y. Yang, D. Liu, A. J. Liang, Q. N. Xu, J. Kroder, V. Süß, H. Borrmann, C. Shekhar, Z. S. Wang, C. Y. Xi, W. H. Wang, W. Schnelle, S. Wirth, Y. L. Chen, S. T. B. Goennenwein, C. Felser, *Nat. Phys.* **2018**, *14*, 1125.
[12] H. Chen, Y. Q. Xing, H. X. Tan, L. Huang, Q. Zheng, Z. H. Huang, X. H. Han, B. Hu, Y. H. Ye, Y. Li, Y. Xiao, H. C. Lei, X. G. Qiu, E. K. Liu, H. T. Yang, Z. Q. Wang, B. H. Yan, H. J. Gao, *Nat. Commun.* **2024**, *15*, 2301.
[13] N. Morali, R. Batabyal, P. K. Nag, E. K. Liu, Q. A. Xu, Y. Sun, B. H. Yan, C. Felser, N. Avraham, H. Beidenkopf, *Science* **2019**, *365*, 1286.
[14] D. F. Liu, A. J. Liang, E. K. Liu, Q. N. Xu, Y. W. Li, C. Chen, D. Pei, W. J. Shi, S. K. Mo, P. Dudin, T. Kim, C. Cacho, G. Li, Y. Sun, L. X. Yang, Z. K. Liu, S. S. P. Parkin, C. Felser, Y. L. Chen, *Science* **2019**, *365*, 1282.
[15] L. Muechler, E. K. Liu, J. Gayles, Q. N. Xu, C. Felser, Y. Sun, *Phys. Rev. B* **2020**, *101*, 115106.
[16] S. N. Guin, P. Vir, Y. Zhang, N. Kumar, S. J. Watzman, C. G. Fu, E. K. Liu, K. Manna, W. Schnelle, J. Gooth, C. Shekhar, Y. Sun, C. Felser, *Adv. Mater.* **2019**, *31*, 1806622.
[17] N. Chowdhury, K. I. A. Khan, H. Bangar, P. Gupta, R. S. Yadav, R. Agarwal, A. Kumar, P. K. Muduli, *Proc. Natl. Acad. Sci. USA* **2023**, *93*, 477.
[18] K.-H. Jin, W. Jiang, G. Sethi, F. Liu, *Nanoscale* **2023**, *15*, 12787.
[19] F. D. M. Haldane, *Phys. Rev. Lett.* **2004**, *93*, 206602.
[20] X. Di, M. C. Chang, N. Qian, *Rev. Mod. Phys.* **2010**, *82*, 1959.
[21] J. L. Shen, Q. Q. Zeng, S. Zhang, H. Y. Sun, Q. S. Yao, X. K. Xi, W. H. Wang, G. H. Wu, B. G. Shen, Q. H. Liu, E. K. Liu, *Adv. Funct. Mater.* **2020**, *30*, 200830.
[22] C. Shekhar, A. K. Nayak, Y. Sun, M. Schmidt, M. Nicklas, I. Leermakers, U. Zeitler, Y. Skourski, J. Wosnitza, Z. K. Liu, Y. L. Chen, W. Schnelle, H. Borrmann, Y. Grin, C. Felser, B. H. Yan, *Nat. Phys.* **2015**, *11*, 645.
[23] Y. W. Liu, X. Yuan, C. Zhang, Z. Jin, A. Narayan, C. Luo, Z. G. Chen, L. Yang, J. Zou, X. Wu, S. Sanvito, Z. C. Xia, L. Li, Z. Wang, F. X. Xiu, *Nat. Commun.* **2016**, *7*, 12516.
[24] T. Neupert, M. M. Denner, J. X. Yin, R. Thomale, M. Z. Hasan, *Nat. Phys.* **2022**, *18*, 137.
[25] H. Chen, H. T. Yang, B. Hu, Z. Zhao, J. Yuan, Y. Q. Xing, G. J. Qian, Z. H. Huang, G. Li, Y. H. Ye, S. Ma, S. L. Ni, H. Zhang, Q. W. Yin, C. S. Gong, Z. J. Tu, H. C. Lei, H. X. Tan, S. Zhou, C. M. Shen, X. L. Dong, B. H. Yan, Z. Q. Wang, H. J. Gao, *Nature* **2021**, *599*, 222.
[26] J. C. Lei, Y. Xie, A. Kutana, K. V. Bets, B. I. Yakobson, *J. Am. Chem. Soc.* **2022**, *144*, 7497.
[27] X. J. Zhou, S. L. He, G. D. Liu, L. Zhao, L. Yu, W. T. Zhang, *Rep. Prog. Phys.* **2018**, *81*, 062101.
[28] I. Belopolski, T. A. Cochran, X. X. Liu, Z. J. Cheng, X. P. Yang, Z. Guguchia, S. S. Tsirkin, J. X. Yin, P. Vir, G. S. Thakur, S. S. Zhang, J. Y. Zhang, K. Kaznatcheev, G. M. Cheng, G. Q. Chang, D. Multer, N. Shumiya, M. Litskevich, E. Vescovo, T. K. Kim, C. Cacho, N. Yao, C. Felser, T. Neupert, M. Z. Hasan, *Phys. Rev. Lett.* **2021**, *127*, 256403.
[29] M. H. Pan, X. Zhang, Y. N. Zhou, P. D. Wang, Q. Bian, H. Liu, X. Y. Wang, X. Y. Li, A. X. Chen, X. X. Lei, S. J. Li, Z. W. Cheng, Z. B. Shao, H. X. Ding, J. Z. Gao, F. S. Li, F. Liu, *Phys. Rev. Lett.* **2023**, *130*, 036203.
[30] D. Kim, F. Liu, *Phys. Rev. B* **2023**, *107*, 205130.
[31] J.-X. Yin, S. S. Zhang, G. Q. Chang, Q. Wang, S. S. Tsirkin, Z. Guguchia, B. Lian, H. B. Zhou, K. Jiang, I. Belopolski, N. Shumiya, D. Multer, M. Litskevich, T. A. Cochran, H. Lin, Z. Q. Wang, T. Neupert, S. Jia, H. C. Lei, M. Z. Hasan, *Nat. Phys.* **2019**, *15*, 443.
[32] S. Y. Yang, J. Noky, J. Gayles, F. K. Dejene, Y. Sun, M. Dörr, Y. Skourski, C. Felser, M. N. Ali, E. Liu, S. S. P. Parkin, *Nano Lett.* **2020**, *20*, 7860.
[33] F. F. Tafti, Q. D. Gibson, S. K. Kushwaha, N. Haldolaarachchige, R. J. Cava, *Nat. Phys.* **2016**, *12*, 272.
[34] C. L. Zhang, C. Guo, H. Lu, X. Zhang, Z. J. Yuan, Z. Q. Lin, J. F. Wang, S. Jia, *Phys. Rev. B* **2015**, *92*, 041203.
[35] M. Tanaka, Y. Fujishiro, M. Mogi, Y. Kaneko, T. Yokosawa, N. Kanazawa, S. Minami, T. Koretsune, R. Arita, S. Tarucha, M. Yamamoto, Y. Tokura, *Nano Lett.* **2020**, *20*, 7476.
[36] L. C. Ding, J. Koo, C. J. Yi, L. C. Xu, H. K. Zuo, M. Yang, Y. G. Shi, B. H. Yan, K. Behnia, Z. W. Zhu, *J. Phys. D Appl. Phys.* **2021**, *54*, 454003.
[37] B. Y. Jiang, L. J. Y. Wang, R. Bi, J. W. Fan, J. J. Zhao, D. P. Yu, Z. L. Li, X. S. Wu, *Phys. Rev. Lett.* **2021**, *126*, 236601.
[38] C. Liu, Y. C. Wang, M. Yang, J. H. Mao, H. Li, Y. X. Li, J. H. Li, H. P. Zhu, J. F. Wang, L. Li, Y. Wu, Y. Xu, J. S. Zhang, Y. Y. Wang, *Nat. Commun.* **2021**, *12*, 4647.

[39] M. Hirschberger, S. Kushwaha, Z. J. Wang, Q. Gibson, S. H. Liang, C. A. Belvin, B. A. Bernevig, R. J. Cava, N. P. Ong, *Nat. Mater.* **2016**, *15*, 1161.

[40] I. Belopolski, K. Manna, D. S. Sanchez, G. Q. Chang, B. Ernst, J. X. Yin, S. S. Zhang, T. Cochran, N. Shumiya, H. Zheng, B. Singh, G. Bian, D. Multer, M. Litskevich, X. T. Zhou, S. M. Huang, B. K. Wang, T. R. Chang, S. Y. Xu, A. Bansil, C. Felser, H. Lin, M. Z. Hasan, *Science* **2019**, *365*, 1278.

[41] J. L. Shen, Q. Q. Zeng, S. Zhang, W. Tong, L. S. Ling, C. Y. Xi, Z. S. Wang, E. K. Liu, W. H. Wang, G. H. Wu, B. G. Shen, *Appl. Phys. Lett.* **2020**, *116*, 029901.

[42] T. Suzuki, R. Chisnell, A. Devarakonda, Y. T. Liu, W. Feng, D. Xiao, J. W. Lynn, J. G. Checkelsky, *Nat. Phys.* **2016**, *12*, 1119.

[43] J. L. Zhang, L. Jin, J. Chen, C. H. Zhang, P. Li, Y. Yuan, Y. Wen, Q. Zhang, X. M. Zhang, E. K. Liu, W. H. Wang, X. X. Zhang, *New J. Phys.* **2021**, *23*, 083041.

[44] K. Kim, J. Seo, E. Lee, K. T. Ko, B. S. Kim, B. G. Jang, J. M. Ok, J. Lee, Y. J. Jo, W. Kang, J. H. Shim, C. Kim, H. W. Yeom, B. I. Min, B. J. Yang, J. S. Kim, *Nat. Mater.* **2018**, *17*, 794.

[45] S. S. Liu, X. Yuan, Y. C. Zhou, Y. Sheng, C. Huang, E. Z. Zhang, J. W. Ling, Y. W. Liu, W. Y. Wang, C. Zhang, J. Zou, K. Y. Wang, F. X. Xiu, *NPJ 2D Mater. Appl.* **2017**, *1*, 37.

[46] X. K. Li, L. C. Xu, L. C. Ding, J. H. Wang, M. S. Shen, X. F. Lu, Z. W. Zhu, K. Behnia, *Phys. Rev. Lett.* **2017**, *119*, 056601.

[47] S. Nakatsuji, N. Kiyohara, T. Higo, *Nature* **2015**, *527*, 212.

[48] H. Li, B. Ding, J. Chen, Z. F. Li, Z. P. Hou, E. K. Liu, H. W. Zhang, X. K. Xi, G. H. Wu, W. H. Wang, *Appl. Phys. Lett.* **2019**, *114*, 192408.

[49] Z. Fang, N. Nagaosa, K. S. Takahashi, A. Asamitsu, R. Mathieu, T. Ogasawara, H. Yamada, M. Kawasaki, Y. Tokura, K. Terakura, *Science* **2003**, *302*, 92.

[50] A. A. Burkov, *Phys. Rev. Lett.* **2014**, *113*, 187202.

[51] Z. Liu, F. Liu, Y. S. Wu, *Chinese Phys. B* **2014**, *23*, 077308.

[52] E. Dagotto, *Science* **2005**, *309*, 257.

[53] Z. Liu, F. Liu, Y. S. Wu, *Phys. Rev. B* **2023**, *108*, 155126.

[54] Y. S. Dedkov, M. Holder, S. L. Molodtsov, H. Rosner, *J. Phys. Conf. Ser.* **2008**, *100*, 072011.

[55] G. Kresse, J. Furthmuller, *Phys. Rev. B* **1996**, *54*, 11169.

[56] J. P. Perdew, K. Burke, M. Ernzerhof, *Phys. Rev. Lett.* **1996**, *77*, 3865.

[57] H. J. Monkhorst, J. D. Pack, *Phys. Rev. B* **1976**, *13*, 5188.

[58] G. Pizzi, V. Vitale, R. Arita, S. Blügel, F. Freimuth, G. Géranton, M. Gibertini, D. Gresch, C. Johnson, T. Koretsune, J. Ibáñez-Azpiroz, H. Lee, J.-M. Lihm, D. Marchand, A. Marrazzo, Y. Mokrousov, J. I. Mustafa, Y. Nohara, Y. Nomura, L. Paulatto, S. Poncé, T. Ponweiser, J. F. Qiao, F. Thöle, S. S. Tsirkin, M. Wierzbowska, N. Marzari, D. Vanderbilt, I. Souza, A. A. Mostofi, et al., *J. Phys.: Condens. Matter* **2020**, *32*, 165902.

[59] Q. S. Wu, S. N. Zhang, H. F. Song, M. Troyer, A. A. Soluyanov, *Comput. Phys. Commun.* **2018**, *224*, 405.

[60] D. Xiao, M. C. Chang, Q. Niu, *Rev. Mod. Phys.* **2010**, *82*, 1959.